View metadata, citation and similar papers at core.ac.uk
brought to you by CORE
provided by Elsevier - Publisher Connector

Solid-State Electronics 74 (2012) 49–57

Contents lists available at SciVerse ScienceDirect

Solid-State Electronics

journal homepage: www.elsevier.com/locate/sse

PNP PIN bipolar phototransistors for high-speed applications built in a 180 nm CMOS process

P. Kostov *, W. Gaberl, M. Hofbauer, H. Zimmermann

Institute of Electrodynamics, Microwave and Circuit Engineering, Vienna University of Technology, Gusshausstr. 25/354, 1040 Vienna, Austria

ARTICLE INFO

Article history:
Available online 14 May 2012

Keywords:
PNP
PIN
Integrated phototransistor
Light detector
Silicon
Photodetector

ABSTRACT

This work reports on three speed optimized pnp bipolar phototransistors build in a standard 180 nm CMOS process using a special starting wafer. The starting wafer consists of a low doped p epitaxial layer on top of the p substrate. This low doped p epitaxial layer leads to a thick space-charge region between base and collector and thus to a high −3 dB bandwidth at low collector–emitter voltages. For a further increase of the bandwidth the presented phototransistors were designed with small emitter areas resulting in a small base-emitter capacitance. The three presented phototransistors were implemented in sizes of $40 \times 40\ \mu m^2$ and $100 \times 100\ \mu m^2$. Optical DC and AC measurements at 410 nm, 675 nm and 850 nm were done for phototransistor characterization. Due to the speed optimized design and the layer structure of the phototransistors, bandwidths up to 76.9 MHz and dynamic responsivities up to 2.89 A/W were achieved. Furthermore simulations of the electric field strength and space-charge regions were done.

© 2012 Elsevier Ltd. Open access under CC BY-NC-ND license.

1. Introduction

Photodiodes and phototransistors are the most commonly used photodetectors. By providing an additional gain, phototransistors are more suitable in some applications than photodiodes like for instance in low light scenarios. Nowadays photodetectors are built in silicon processes (these can also be standard CMOS or BiCMOS processes) or as III–V compound devices. Photodetectors integrated into standard silicon-based processes have several advantages over photodetectors realized in special silicon or III-V compound technologies. The main advantage of the implementation into a standard silicon process is the possibility for a cheap mass production of detector and circuitry together. The potential to combine the photodetector together with the readout circuitry to optoelectronic integrated circuits (OEICs) introduces further advantages of integrated solutions over wire-bonded solutions, due to the absence of bonding pads and bonding wires leading to less parasitic [1].

The physical property of silicon allows the material to be sensitive for wavelengths between 300 nm and 1100 nm. Light within this wavelength range will penetrate into the silicon and will be absorbed in it. Depending on the wavelength of the light, each photon can create one or more electron–hole pairs. A photon can create more than one electron–hole pair only if it is a high energy photon (corresponds to wavelengths below 375 nm) [2,3]. However, the photon can also be absorbed by free carriers without generating an electron–hole pair (free carrier absorption) [4]. Nevertheless, if silicon photodetectors are used in the visible and near-infrared range (400–900 nm), literature shows, that both mentioned effects can be neglected. Therefore for the visible light range the generation rate G of electron–hole pares in silicon can be simplified to [1]:

$$G(x, \lambda) = \Phi_0 \alpha(\lambda) e^{-\alpha(\lambda)x} \quad (1)$$

The generation rate G is dependent on the depth x from the semiconductor surface, on the wavelength λ, on the photon flux Φ_0 of the incident light and on the absorption coefficient α. The absorption coefficient α decreases strongly for increasing wavelength λ. To give two relevant examples: blue light (e.g. 430 nm) is absorbed in depths up to 0.2 μm while near infrared light (e.g. 850 nm) has a $1/e$ penetration depth of about 16.6 μm [1]. In a biased photodetector the electrical field separates the carriers. The wavelength dependent penetration depths lead to a wavelength dependent distribution of the total photocurrent into a drift and diffusion part, which further leads to wavelength dependent bandwidths and responsivities.

Photodiodes are the most common photodetectors. They can be implemented as a pn-junction or a pin-junction device. The difference between both structures is the additional low doped layer in the pin photodiode. In the junction region of the photodiode a space-charge region is formed. The space-charge region is thicker for the pin photodiode due to the additional low doped layer between the anode and cathode. For a vertical pin photodiode this

* Corresponding author. Tel.: +43 1 58801 354624; fax: +43 1 58801 9354624.
E-mail addresses: plamen.kostov@tuwien.ac.at (P. Kostov), wolfgang.gaberl@tuwien.ac.at (W. Gaberl), michael.hofbauer@tuwien.ac.at (M. Hofbauer), horst.zimmermann@tuwien.ac.at (H. Zimmermann).

0038-1101 © 2012 Elsevier Ltd. Open access under CC BY-NC-ND license.
http://dx.doi.org/10.1016/j.sse.2012.04.011

will lead to a higher responsivity for deeper penetrating light and typically to a higher bandwidth since the drift current part is increased. PN photodiodes can be built in three different ways in a standard CMOS process using a p wafer: n-well/p-substrate, n+/p-substrate and p+/n-well. These diodes are characterized by a thin space-charge region and thus a small drift photocurrent, which leads to a relatively small bandwidth due to a large contribution of a diffusion current from photocharges generated below the space-charge region. However, by adding a thick intrinsic layer between the photodiode's anode and cathode, a thick space-charge region is formed and thus also a thick drift zone. A thicker drift zone leads to a larger fraction of drift current compared to diffusion current, which leads furthermore to higher bandwidths for low bias voltages. The advantage of higher bandwidths in pin over pn photodiodes makes them the most commonly used detector for high speed optical applications, for example in optical receivers [5]. Such a vertical pin photodiode with a −3 dB bandwidth of 2.8 GHz at $V_D = 20$ V and 0.2 A/W for 850 nm responsivity is presented in [6]. Another vertical pin photodiode with a responsivity of 0.135 A/W for 850 nm and a bandwidth of 1.6 GHz at $V_D = 15.5$ V is presented in [7] Furthermore pin photodiodes can also be implemented as lateral devices. In [7] lateral pin photodiodes with responsivities up to 0.15 A/W for 850 nm and bandwidths up to 3.1 GHz at $V_D = 15.5$ V are presented. For comparison the pn photodiodes presented in [8] reach a bandwidth of 80 MHz at $V_D = 8$ V and responsivities of 0.215 A/W and 0.15 A/W for 650 nm. As can be seen on the presented values, photodiodes can achieve only small responsivities in the range of 600–800 nm. This is due to a maximum quantum efficiency of $\eta = 1$. However, the maximum quantum efficiency cannot be reached in real devices due to reflection of the light at the surface as well as recombination of the photogenerated charges in the silicon.

Photodetectors with an inherent current amplification are introduced by avalanche photodiodes and phototransistors. Due to their inherent current amplification these photosensitive devices can improve the quantum efficiency limitation of photodiodes and reach values for η larger than 1.

Avalanche photodiodes achieve their inherent current amplification by an avalanche multiplication process. The drawback of this process is that voltages in the range of several tens of volts are needed to achieve sufficient electrical field strength for the inherent current amplification [9]. High voltages are a problem in integrated circuits and even more in modern low-voltage processes. However, new kinds of avalanche photodiodes, so called SPADs (single-photon avalanche photodiodes), can operate at smaller voltages than the standard avalanche photodiodes. In [10] two kinds of SPADs are presented with break-down voltages of 23.1 V and 16.1 V, respectively. The very narrow bias voltage range for linear operation of APDs and SPADs is a further disadvantage of these kinds of photodetectors.

Phototransistors have the big advantage over APDs that they do not need high voltages for their inherent current amplification. In BiCMOS, quite fast vertical npn phototransistors with responsivities of 2.7 A/W at 850 nm (due to the thin base–collector space-charge region) were reported [11]. Another BiCMOS SiGe phototransistor with a responsivity of 5.2 A/W at 850 nm is presented in [12]. In CMOS technology different types of phototransistors can be built, e.g. vertical bipolar phototransistors [13–18], lateral bipolar phototransistors [19], photo-MOSFETs [20], and so on. Vertical bipolar phototransistors with bandwidths up to 14 MHz and responsivities up to 98 A/W at 675 nm are presented in [13] and [14]. The CMOS lock-in amplifier presented in [15] uses pnp phototransistors with bandwidths of a few 100 kHz. Ref. [16] describes a pnp phototransistor with a bandwidth of 7.8 MHz at 638 nm. In [17] a photodiode and a npn phototransistor in a 65 nm CMOS process are presented. The phototransistor achieves a responsivity of 0.34 A/W and a bandwidth of 150 kHz. This work describes extended results of the phototransistors presented in [18].

2. Working principle

A vertical pnp phototransistor is formed in a CMOS process by implementing an n-well (base) in the p-substrate (collector) and a p^+-source/drain (emitter) in the n-well. Fig. 1a depicts the cross-section of a conventional pnp bipolar phototransistor. The pnp phototransistor can be used only in emitter-follower configuration since the substrate forms the collector. The phototransistor can be described as a photodiode (base–collector junction) and an internal bipolar junction transistor for the current amplification. Light with long wavelength penetrates deep into silicon and generates most charges in the base–collector space-charge region. There the charges are separated and electrons are swept into the base and holes into the collector. The electron accumulation in the base makes the potential of the base more negative, thus the forward bias voltage of the base-emitter diode increases and injection of holes from the emitter into the base becomes stronger. A large part of the injected holes can diffuse through the thin base and reach the base–collector space-charge region at the other end of the base area. This process leads to the amplification of the primary photocurrent. The inherent current amplification β is the relation between the collector current I_C and the primary photocurrent I_{PH}. Further literature on conventional CMOS phototransistors can be found in [1,21,22].

3. Methodology

We present three speed optimized pnp PIN phototransistors with sizes of $40 \times 40\ \mu m^2$ and $100 \times 100\ \mu m^2$. The phototransistors are built in a 180 nm CMOS process without any process modification and have been fabricated by LFoundry. For achieving high bandwidths a special wafer was used. This wafer consists of a p^+ substrate with a low doped ($5 \times 10^{13}\ cm^{-3}$) p epitaxial layer grown with a thickness of 15 μm on it. A thick base–collector space-charge region is formed therefore even at low voltages due to the present low doped p epitaxial layer. The PIN structure of the base–collector diode has the same properties like the mentioned PIN photodiodes in Section 1 and leads therefore to a fast separation of the photogenerated charges. As a consequence of the thick space-charge region the drift portion of the photocurrent for deep penetrating light rises and leads therefore to a higher responsivity compared to a conventional bipolar phototransistor like the one presented in [15].

The bandwidths and the responsivities of the phototransistors depend also on the layout properties of the base and emitter area. Eq. (2) shows the relationship between the −3 dB bandwidth of the phototransistor and the physical properties of the phototransistor [21]:

$$f_{-3dB} = \frac{1}{2\pi\beta \cdot \left(\tau_B + \frac{k_B T}{q I_E}(C_{BE} + C_{BC})\right)}, \tag{2}$$

where f_{-3dB} is the −3 dB bandwidth of the phototransistor, β is the forward current gain of the phototransistor, τ_B is the base transit time, k_B is the Boltzmann constant, T is the absolute temperature, q is the elementary charge, I_E is the emitter current of the phototransistor, C_{BE} is the base-emitter capacitance and C_{BC} is the base–collector capacitance.

The −3 dB bandwidth depends on both space-charge region capacitances C_{BE} and C_{BC}, current gain β, base transit time τ_B and the emitter current I_E. In case of large capacitance values the −3 dB bandwidth is mainly dependent on both space-charge region capacitances C_{BE} and C_{BC}. For fast phototransistors a reduction

of these capacitances is desired. In our presented phototransistors the capacitance C_{BC} is small compared to common phototransistors (e.g. Fig. 1a) due to the implemented thick low doped p epitaxial layer. Furthermore, a diminution of the capacitance C_{BE} is achieved by reducing the emitter area. Regarding the base doping two contrary effects have to be mentioned. On the one hand a reduction of the doping concentration in the base can lead to an increase of the bandwidth since both space-charge regions will reach deeper into the base leading to wider space-charge regions and thus smaller capacitances C_{BE} and C_{BC}. As a second consequence of larger space-charge region, the effective base width W becomes shorter leading to a reduced base transit time τ_B and thus also to an increased bandwidth. On the other hand, thicker space-charge regions will cause a reduction of the electric field strength inside the space-charge regions for the same potential conditions, leading to a slower device since the velocity of the charge carriers in the space-charge region will be reduced. This can be seen from the simulations in Section 5.1. Furthermore the reduction of the base doping concentration leads to a higher inherent current gain β and thus to a higher collector and emitter current I_C and I_E. The higher emitter current will cause according Eq. (2) a higher bandwidth. Hence it follows that for phototransistors with generally small junction capacitances (e.g. optimized emitter layout, PIN structure) the frequency behavior of the device becomes more dependent on the other parameters like β, τ_B and I_E. A further increase of the bandwidth can be achieved by reducing the existing perimeter capacitance and further by reducing the size of the whole phototransistor. A reduction of the perimeter capacitance was achieved by adding a 3 μm gap with low doping between the n-well base and the p-well collector contact. However, the bandwidth of the PIN phototransistor is lower than the bandwidth of the PIN photodiode due to the both junction capacitances and the base transit time τ_B which is no issue in the photodiode.

As mentioned above, the bandwidth will increase when reducing the emitter area. On the other side, a smaller emitter area results in a smaller responsivity if the whole device is illuminated. The reason for the smaller responsivity is the higher charge recombination probability due to a longer travel distance. Charges which are not generated directly under the emitter have to travel longer distances through the base to reach the base-emitter junction. These charges will contribute to the photocurrent only if their lifetimes are longer than the time they need to reach the base-emitter space-charge region. Regarding the responsivity the base doping concentration plays also a crucial role. For a smaller base doping concentration a thinner effective base width W is formed leading to a decreased travel distance of the generated charges through the base. This increases the probability for the charges to reach the base-emitter junction and thus also increases the inherent current amplification β. The inherent current amplification β is proportional to the emitter doping concentration N_E and the Gummel number N_G, which describes the doping concentration N_B of the base [22]:

$$N_G = \int_0^w N_B(x)dx, \tag{3}$$

$$\beta \propto \frac{N_E}{N_G} \tag{4}$$

As a consequence we can say that for achieving high responsivities the phototransistors should be designed with a large emitter over the whole photosensitive area together with a low doped base. Whereas for achieving higher bandwidths the phototransistors should be designed with very small emitter areas together with tendencially higher doped bases. It should be furthermore mentioned that by reducing the doping concentration of the base the probability for reach-through between collector and emitter increases, which should be avoided. However, the presented phototransistors are designed for high bandwidth applications and are implemented thus with small emitter areas. In the measurement section of this paper it can be seen that no reach-through arises for even high collector–emitter voltages.

4. Implemented phototransistors

The three realized phototransistor versions (Fig. 1b–d) were built in 40 × 40 μm^2 and 100 × 100 μm^2 and have due to different layout designs of base and emitter different characteristics:

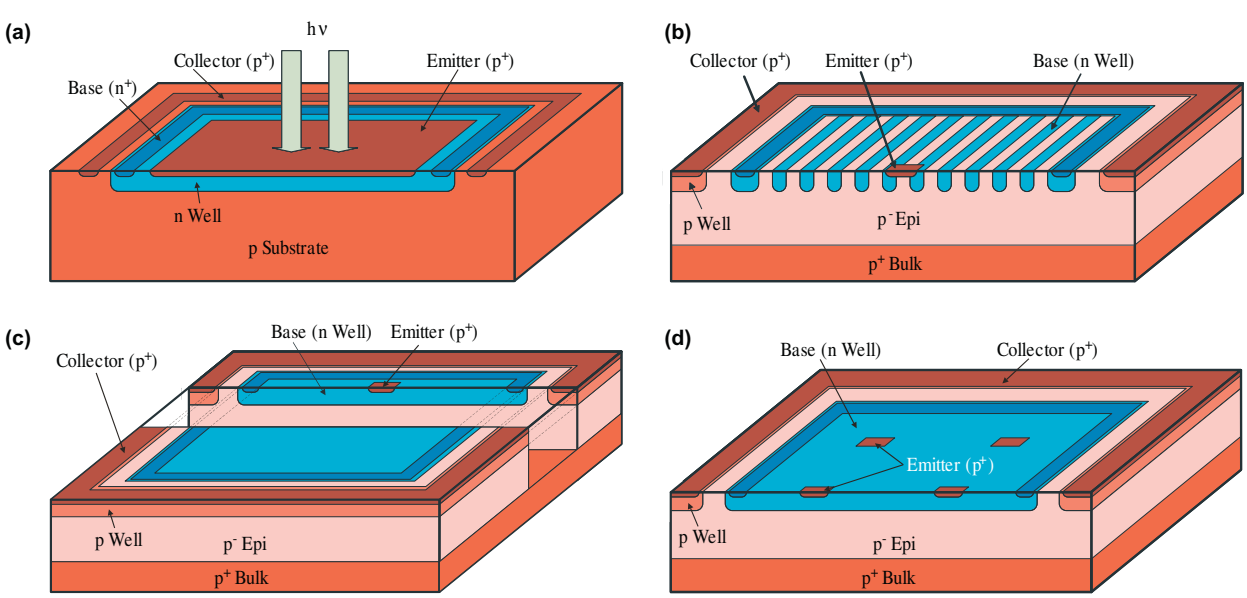

Fig. 1. 3D depiction and cross section of the phototransistors: (a) common pnp phototransistor integrated in CMOS technology, PIN PNP phototransistors: (b) $50_B Center_E$, (c) $100_B Edge_E$ and (d) $100_B Quad_E$.

- *$50_B Center_E$*: This phototransistor was designed with a striped base. These n-well stripes have a width of 0.5 μm and are separated by 0.5 μm wide gaps between them. During the fabrication the n-well stripes will diffuse due to the thermal budget into one single layer with the half doping concentration of a base consisting of a full n-well. This is also the reason why this device is called $50_B Center_E$. The emitter of this device has the size of 0.74 × 0.74 μm^2 and is placed in the center of the photosensitive area.
- *$100_B Edge_E$*: As can be seen from the name, this device consists of a full n-well base and an emitter at the edge of the photosensitive area. It has a slightly larger emitter area compared to the $50_B Center_E$ phototransistor due to the demands of the design rule specifications. The emitter area has a size of 2.18 × 0.32 μm^2 and is formed by a p^+ drain/source implant. The idea for having the emitter at the edge of the photosensitive area is based on the idea of implementing an anti-reflection layer and an optical window etch on top of the photosensitive area and thus increasing the responsivity of the device. However, for a better comparison devices without an optical window edge were used.
- *$100_B Quad_E$*: This device has a similar layout as the device presented before. The difference between both phototransistors is that this device has four separate emitter areas. Each emitter area is placed in the center of each quadrant of the photosensitive area. All emitter areas are connected with minimum width metal lines on top of the phototransistor.

5. Results and discussion

We characterized the presented phototransistors by optical DC and AC measurements. Optical DC measurements were done using a laser with 850 nm wavelength for the characterization of the phototransistors output characteristic and DC responsivity. Also, the spectral responsivity over the whole visible light spectrum was measured. Dynamic responsivity and bandwidth measurements of the phototransistors were done at 410 nm, 675 nm and 850 nm, respectively. The following equipment was used for the characterization of the phototransistors: the three mentioned laser sources, a monochromator for measuring the spectral responsivity, an optical attenuator and optical power meter for monitoring the light power, source-meter-units (SMUs) for applying voltages and measuring current, an oscilloscope for measuring the AC responsivity and a vector network analyzer for measuring the frequency step response, respectively. All optical paths were calibrated with a fast optical reference photodiode. Furthermore the electric field strength and the space-charge regions of the phototransistors were simulated.

5.1. Electric field strength and space-charge region simulation

Electric field strength and space-charge region simulations were done in order to make clear the variations between different collector–emitter voltages V_{CE} and different base doping concentrations. The phototransistor $50_B Center_E$ was simulated in dark light conditions at V_{CE} = −2 V, −5 V and −10 V always with floating base. Fig. 2 depicts the electric field strength in this phototransistor. In this figure the thick drift zone of the base–collector space-charge region and the strength of the electric field are noticeable. The peaks close to Y = 0 μm are due to the contacts of collector, base and emitter of the phototransistor. For a better comparison of the electric field strength in the base–collector space-charge region for the three collector–emitter voltages the electric field strength was limited in the plot. Strong electric field strength peaks in the contact region are not shown to improve the scaling of the overall picture. The electric field strength in the base-emitter space-charge region reaches 35 kV/cm. The borders of the space-charge regions for the $50_B Center_E$ phototransistor are depicted in Fig. 3. The phototransistor was simulated with a single n-well layer with the half doping concentration since the n-well stripes of this device will diffuse during the production into a single layer. Recog-

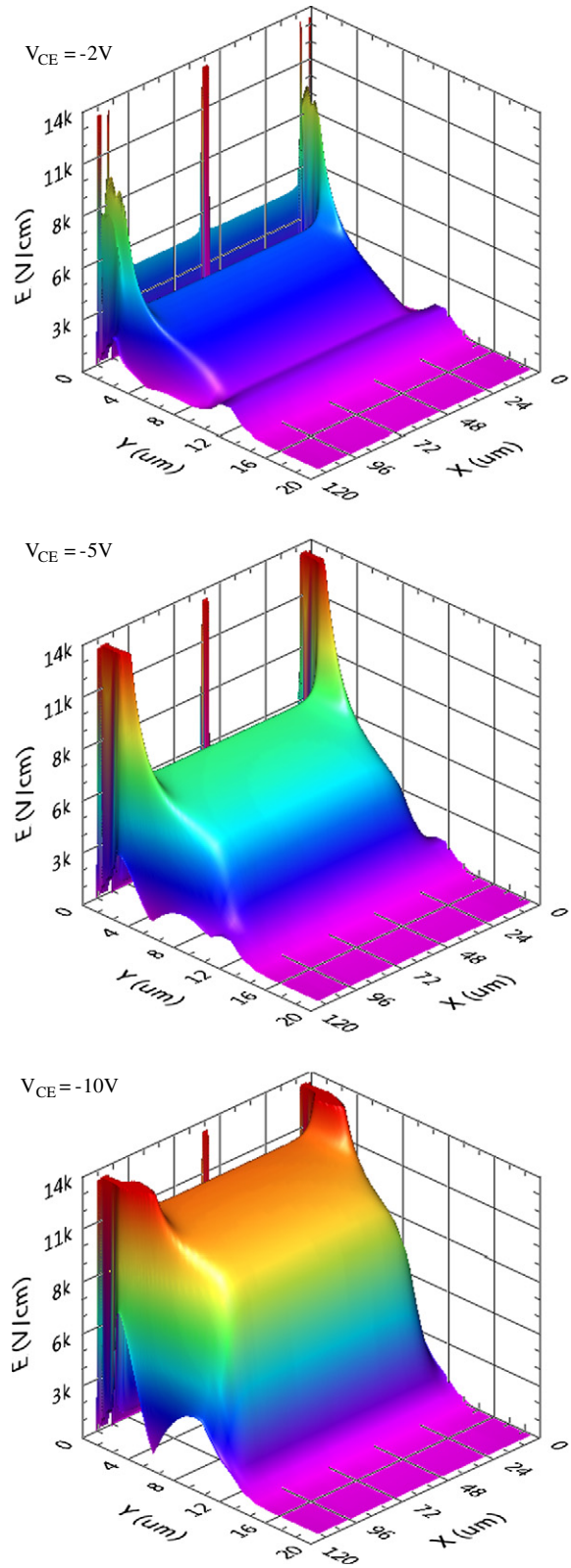

Fig. 2. Simulated electric field strength for the $50_B Center_E$ phototransistor at three different V_{CE} voltages.

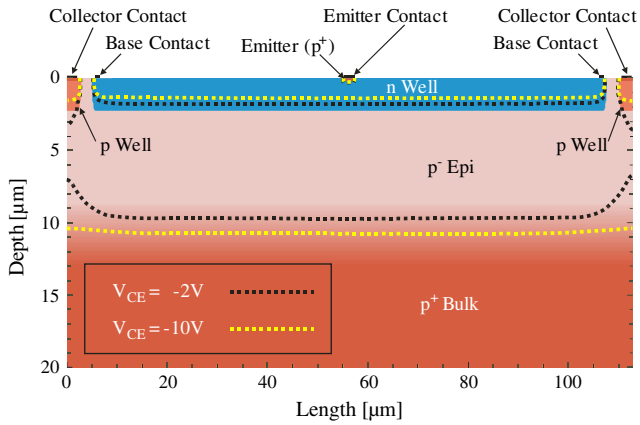

Fig. 3. Borders of the space-charge region at $V_{CE} = -2$ V and -10 V for the $50_B Center_E$ phototransistor.

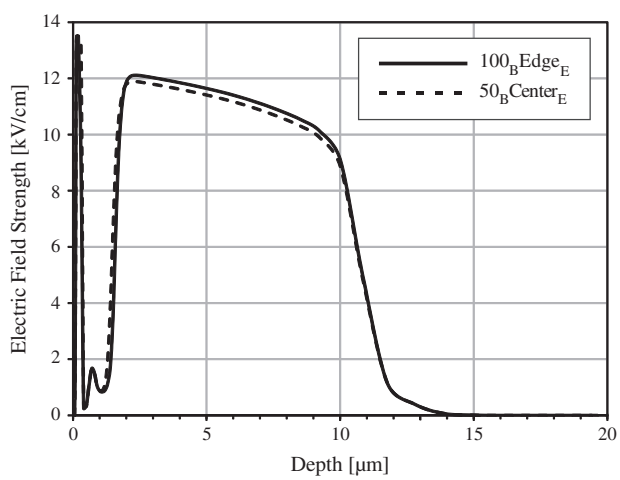

Fig. 4. Cross-section of the electric field strength at the center of the emitter of the $50_B Center_E$ and of the $100_B Edge_E$ phototransistor.

nizable is the difference in the thickness of the base–collector space-charge region due to different collector–emitter voltages. In Fig. 4 the difference of the electric field between the $50_B Center_E$ and $100_B Edge_E$ phototransistor is depicted. Due to the lower doping concentration inside the base it is apparent that the $50_B Center_E$ phototransistor has wider space-charge regions but lower electric field strength compared to the $100_B Edge_E$ phototransistor. Thinner space-charge regions and thus higher electric field strengths in them will lead to a faster drift component. This can be seen in the bandwidth results section (Section 5.3.2).

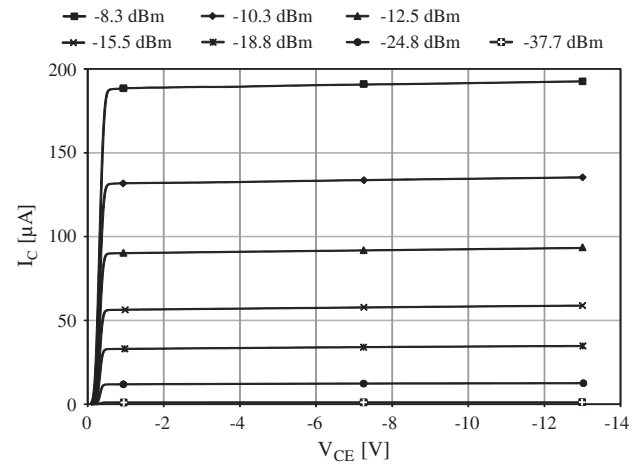

Fig. 5. Output characteristics of the 100×100 µm^2 $50_B Center_E$ phototransistor at 850 nm for different optical power with floating base.

5.2. DC characterization

The DC characterization was split in two different measurement setups. First, the output characteristics were characterized and secondly the spectral responsivity was measured.

5.2.1. I_C vs. V_{CE} curve family and responsivity at 850 nm

For the characterization of the I_C vs. V_{CE} curve family (output characteristics) a light source with 850 nm wavelength was used. The operating point was changed by sweeping the collector–emitter voltage V_{CE} from 0 V to -13 V and the optical power between -37.7 dBm and -8.3 dBm. Thereby the light power was changed by an optical attenuator and monitored via an optical power meter. A source-meter-unit (SMU) was used on one hand to change the collector–emitter voltage and on the other hand to measure the collector current, respectively. The base contact was left floating. Fig. 5 depicts the output characteristics of the 100×100 µm^2 $50_B Center_E$ phototransistor. In this figure, it can be seen that for voltages V_{CE} up to -13 V no reach-through occurs. All other devices show an almost similar output characteristic like the depicted one.

Table 1
DC responsivity in A/W for the three 100×100 µm^2 phototransistors for three different collector–emitter voltages at 850 nm and an optical power of -37.7 dBm and -15.5 dBm.

	$P_{opt} = -37.7$ dBm			$P_{opt} = -15.5$ dBm		
	$V_{CE} = -2$ V	$V_{CE} = -5$ V	$V_{CE} = -10$ V	$V_{CE} = -2$ V	$V_{CE} = -5$ V	$V_{CE} = -10$ V
$50_B Center_E$	6.12	6.23	6.37	2.01	2.03	2.07
$100_B Edge_E$	3.50	3.51	3.52	2.00	2.02	2.05
$100_B Quad_E$	3.57	3.57	3.59	2.63	2.65	2.68

Table 2
Dynamic responsivity in A/W for the three 100×100 µm^2 phototransistors for two different collector–emitter voltages at 410 nm, 675 nm, 850 nm and floating base.

	$\lambda = 410$ nm		$\lambda = 675$ nm		$\lambda = 850$ nm	
	$V_{CE} = -2$ V	$V_{CE} = -10$ V	$V_{CE} = -2$ V	$V_{CE} = -10$ V	$V_{CE} = -2$ V	$V_{CE} = -10$ V
$50_B Center_E$	0.45	0.48	1.93	1.95	1.34	1.36
$100_B Edge_E$	0.47	0.51	2.06	2.08	1.40	1.50
$100_B Quad_E$	0.71	0.74	2.81	2.89	2.20	2.34

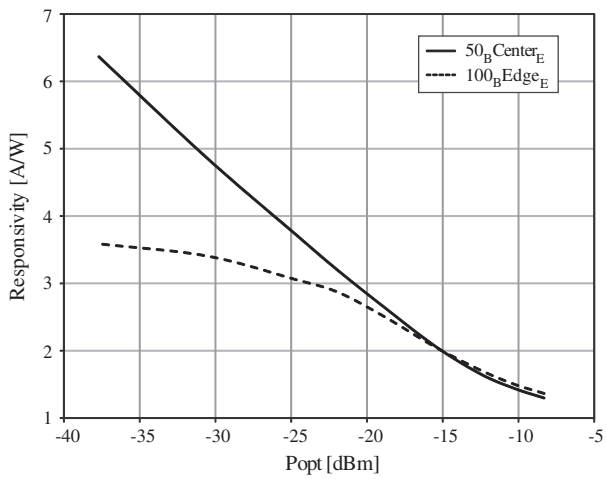

Fig. 6. DC responsivities of the $100 \times 100\ \mu m^2$ $50_BCenter_E$ and 100_BEdge_E phototransistors at 850 nm at $V_{CE} = -10$ V.

The calculated DC responsivity for the $50_BCenter_E$ and the 100_BEdge_E $100 \times 100\ \mu m^2$ phototransistors at $V_{CE} = -10$ V is depicted in Fig. 6. The responsivity decreases for increasing optical light power due to a reduced gain in the phototransistor, which is caused by a change in the operating point as described in [13]. Thereby the higher optical light power induces a high collector current I_C which leads to a current density being larger than the critical current density $j_c \sim N_C$ (N_C is the collector doping concentration) given by the Kirk effect [23,24] (also called base push out effect). Due to the doping concentration of $5 \times 10^{13}\ cm^{-3}$ in the collector layer (this is the thick p-epitaxial layer) instead of usual collector doping levels above $10^{15}\ cm^{-3}$, the critical current density is reduced by about two orders of magnitude. Therefore, even at rather low collector currents, the current gain β reduces with increasing optical input power.

At weak optical light power the $50_BCenter_E$ phototransistor shows a higher gain due to the lower doped base and thus a higher inherent current gain β. Phototransistor 100_BQuad_E has due to more emitter area a little bit higher responsivity as the 100_BEdge_E phototransistor. For all phototransistors the responsivity does not change much for different V_{CE}, since the collector current I_C is less dependent on different V_{CE} in the forward active region (see Fig. 5). In Table 1 the DC responsivities for the three $100 \times 100\ \mu m^2$ phototransistors at different V_{CE} and different optical light power are shown.

5.2.2. Spectral responsivity

The spectral responsivities of the phototransistors were measured by means of a monochromator. It was used to sweep the wavelength of the light from 400 nm to 900 nm. The optical light power of the monochromator changes thereby between −35.7 dBm and −26 dBm as depicted in Fig. 7a. The optical output power of the monochromator with attached optical fiber was measured with a calibrated reference photodiode. Then the fiber was adjusted to the phototransistors, whereby all light fell into their light sensitive area. A SMU was used to set the collector–emitter voltage and to measure the emitter current. The responsivity was then calculated from the measured emitter current and this incident light power. Fig. 7b shows the responsivity of the $50_BCenter_E$ and the 100_BEdge_E $100 \times 100\ \mu m^2$ phototransistors at $V_{CE} = -2$ V. The phototransistor $50_BCenter_E$ shows a higher responsivity compared with the 100_BEdge_E phototransistor (compare with Fig. 6). A maximum responsivity is measured for all phototransistors in the red wavelength range. The oscillations, which can be seen in the spectral responsivity, are due to the influence of optical interference in the full oxide and passivation stack. They can be avoided by applying an optical window etch step together with an antireflection coating on top of the photosensitive area.

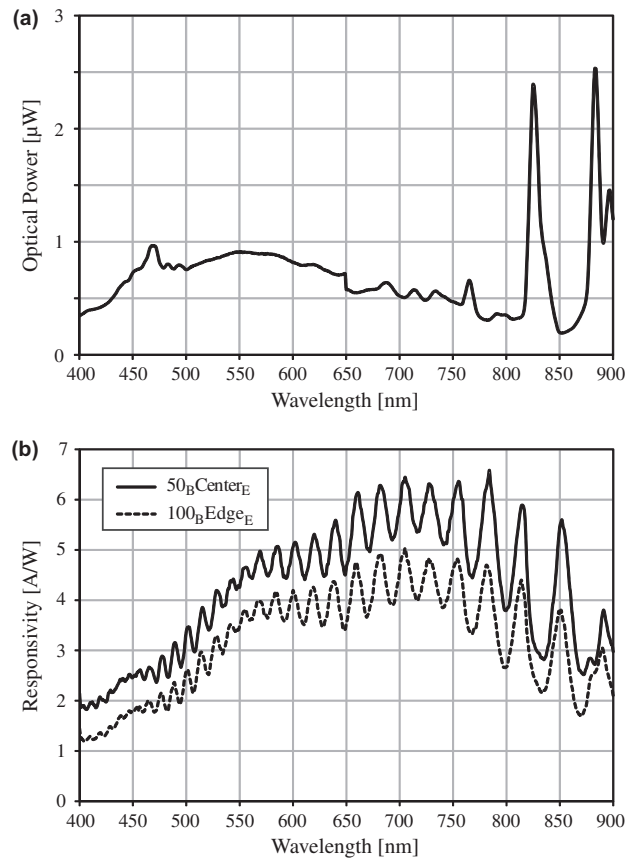

Fig. 7. Spectral measurements: (a) emitted optical power of the monochromator and (b) spectral responsivity of the $100 \times 100\ \mu m^2$ $50_BCenter_E$ and 100_BEdge_E phototransistors at $V_{CE} = -2$ V.

5.3. AC characterization: responsivity and bandwidth

AC responsivity measurements of the phototransistors were done at three different wavelengths: 410 nm, 675 nm and 850 nm. By using the same optical light power for the mentioned wavelengths different collector currents I_C will arise on the one hand due to different responsivities at each wavelength and on the other hand on different energy per photon for different light color. Therefore a comparison of the individual wavelengths would not be absolutely correct since the phototransistor would operate in various operating points for different wavelengths. For a better comparison, an alignment of the optical light power was applied to meet the same collector current I_C. Thus the mean optical light power at 410 nm was set to −12.7 dBm, at 675 nm it was set to −19.2 dBm and at 850 nm it was set to −15.8 dBm. Due to the used laser sources the extinction ratio was 2.00, 2.74 and 1.48 for 410 nm, 675 nm and 850 nm, respectively. During the AC characterization also different operating points were used for the phototransistors. Additionally the collector–emitter voltage V_{CE} was set to −2 V, −5 V and −10 V and the base current I_B was varied from floating condition (0 µA) to 1 µA, 2 µA, 5 µA and 10 µA. A bias-tee element together with an on-chip base-resistor was used to set the different operating points.

5.3.1. AC responsivity

The dynamic responsivity was measured for the three mentioned wavelengths at a frequency of 630 kHz. The phototransistors were connected in emitter follower configuration and their output signal was capacitively coupled to the oscilloscope via a bias tee element. All phototransistors achieve rather small responsivities mainly due to the small emitter areas. These small emitter areas implicate a higher recombination probability of the charges inside the base area. This is caused by the fact that the charges have to travel longer distances to reach the emitter area. Only charges which are generated directly under the emitter have to pass only a short distance through the base to reach the base-emitter space-charge region. However, the phototransistors presented here are designed for achieving high bandwidths. In Table 2 the dynamic responsivities for the different phototransistors at different collector–emitter voltages V_{CE}, floating base and different wavelengths are presented. The highest responsivity of 2.89 A/W is achieved for the $100_B Quad_E$ phototransistor at $V_{CE} = -10$ V and 675 nm. By applying the above mentioned base currents the responsivity slightly decreases. This is caused by an arising base-push out effect and a reduced current gain β due to high base currents [23,24]. Due to the demands of the design rule specifications the $100_B Edge_E$ phototransistor has a slightly larger emitter area which results also in a slightly higher responsivity compared to the $50_B Center_E$ phototransistor.

5.3.2. Bandwidth

The bandwidth characterization of the phototransistors was done by the means of a vector network analyzer (VNA). The phototransistors $50_B Center_E$ and $100_B Edge_E$ show nearly the same bandwidths. Phototransistor $100_B Quad_E$ achieves lower bandwidths due to more emitter area and thus a larger base-emitter capacitance C_{BE}. For the $50_B Center_E$ phototransistor the high bandwidth is mainly caused by the thin effective base width and thus short base transit time and furthermore smaller junction capacitances C_{BC} and C_{BE}. Regarding the $100_B Edge_E$ phototransistor, which is even slightly faster, the high bandwidth is dominated by the slightly higher electric field strength in the space-charge regions. These space-charge regions are slightly smaller due to the higher doped base area. Furthermore the small sized phototransistors show a higher bandwidth compared to the large sized ones. Here the smaller base–collector capacitance and a smaller perimeter capacitance are the main reasons. A higher bandwidth can be achieved by increasing the collector–emitter voltage V_{CE} and also by applying a base current I_B. The higher V_{CE} leads to wider space-charge regions, causing smaller junction capacitances C_{BE} and C_{BC}, and consecutively to a thinner effective base width, causing a shorter base transit time. Furthermore the higher V_{CE} causes a stronger electric field strength inside the device (see Fig. 2). Fig. 8 shows the frequency response dependency on the size of the phototransistors as well as on the collector–emitter voltage V_{CE} at 850 nm for the $100_B Edge_E$ phototransistor. The −3 dB bandwidths are 12.0 MHz and 25.7 MHz for the $100 \times 100\ \mu m^2$ sized phototransistors and 14.2 MHz and 50.7 MHz for the $40 \times 40\ \mu m^2$ sized phototransistors at $V_{CE} = -2$ V and −10 V, respectively.

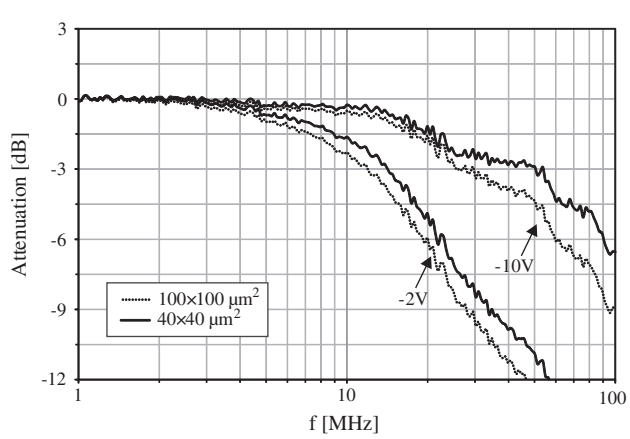

Fig. 8. Frequency response of the $40 \times 40\ \mu m^2$ and $100 \times 100\ \mu m^2$ $100_B Edge_E$ at 850 nm and floating base.

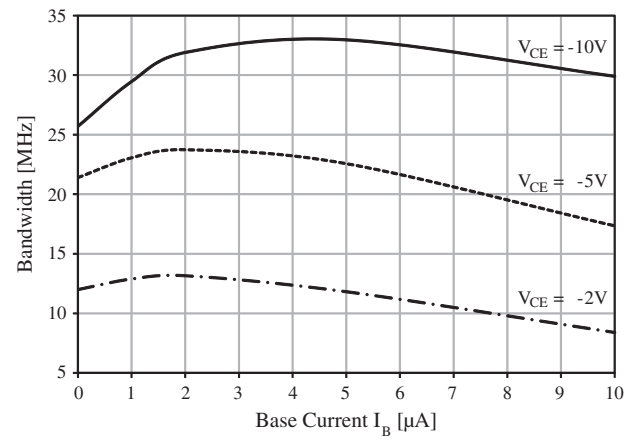

Fig. 9. Bandwidth dependence on base current at three different V_{CE} voltages for the $100 \times 100\ \mu m^2$ $100_B Edge_E$ at 850 nm.

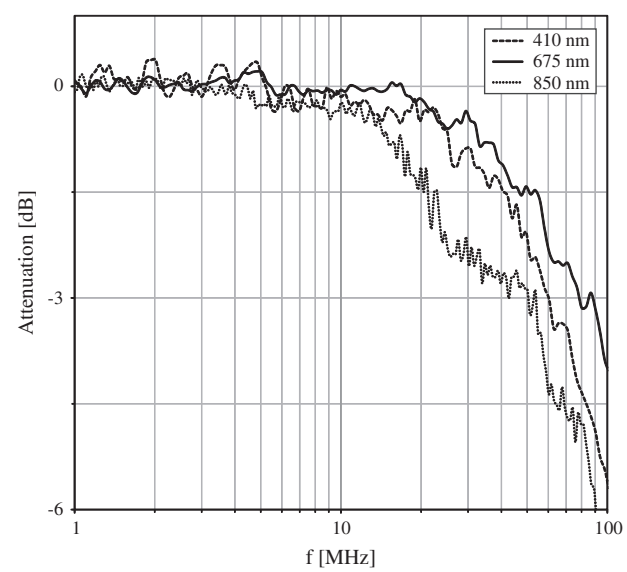

Fig. 10. Frequency response of the $40 \times 40\ \mu m^2$ $100_B Edge_E$ phototransistor at 410 nm, 675 nm, 850 nm and $V_{CE} = -10$ V.

In Fig. 9 the bandwidths for the $100 \times 100\ \mu m^2$ $100_B Edge_E$ phototransistor at 850 nm and different operating points are depicted. The bandwidth increases with the base current until the collector current density reaches a maximum. At this point the largest homogeneous electric field exists in the base–collector space-charge region. By driving a higher collector current the charges cannot be carried completely by the electric field anymore [22]. Beyond the maxima in Fig. 9 the base push-out effect arises and leads to a spreading of the effective base into the collector [23,24]. Thus the effective base width gets wider and the base transit time increases, leading according to Eq. (2) to a reduced bandwidth. However, it should be mentioned that the position of the maxima in Fig. 9 depend on the collector–emitter voltage

Table 3
Bandwidths in MHz of the three presented phototransistors at 410 nm, 675 nm, 850 nm as well as floating base and $V_{CE} = -2$ V and -10 V. The top table presents the values for the $40 \times 40\ \mu m^2$ phototransistors and the bottom table for the $100 \times 100\ \mu m^2$ phototransistors.

	λ = 410 nm		λ = 675 nm		λ = 850 nm	
	$V_{CE} = -2$ V	$V_{CE} = -10$ V	$V_{CE} = -2$ V	$V_{CE} = -10$ V	$V_{CE} = -2$ V	$V_{CE} = -10$ V
$50_B Center_E$	10.7	57.5	9.6	67.0	12.8	50.0
$100_B Edge_E$	14.4	60.5	12.1	76.9	14.2	50.7
$100_B Quad_E$	20.2	54.2	18.8	60.3	18.6	31.6
$50_B Center_E$	9.8	36.5	9.1	54.0	10.5	25.1
$100_B Edge_E$	12.2	40.1	12.0	58.7	12.0	25.7
$100_B Quad_E$	16.6	34.0	16.1	51.6	15.8	21.4

Table 4
Comparison of CMOS and BiCMOS phototransistors at 850 nm.

Refs.	Technology	Device type	Dimension (μm^2)	Wavelength (nm)	P_{opt} (dBm)	Responsivity (A/W)	f_{-3dB} (MHz)	GBW (A/W MHz)
[11]	0.35 μm SiGe HBT BiCMOS	NPN	6 × 10	850	−17	2.7	2000	5400[a]
[12]	0.35 μm SiGe BiCMOS	PNP	21 × 25	850	–	5.2	–	–
[14]	0.6 μm CMOS	PNP	100 × 100	850	−21.2	1.8	14[b]	25.2
[15]	0.35 μm CMOS	PNP	35 × 35	–	–	–	<1	–
[17]	65 nm CMOS	NPN	60 × 60	850	–	0.34	0.15	0.05
This work	0.18 μm CMOS	PNP	100 × 100	850	−15.8	1.5	25.7[b]	38.6
			40 × 40			1.44	50.7[b]	73.0

[a] Small device illuminated with tapered fiber to get a 2.5 μm diameter optical spot.
[b] Fastest device for 850 nm.

V_{CE}. Hence an increase of V_{CE} leads also to an increase of the corresponding maximum collector current density and thus furthermore to an increase of the base current for the bandwidth maximum.

The difference in the bandwidth at different wavelengths for the $40 \times 40\ \mu m^2$ $100_B Edge_E$ phototransistor at $V_{CE} = -10$ V is shown in Fig. 10. The −3 dB bandwidths are 50.7 MHz at 850 nm, 76.9 MHz at 675 nm and 60.5 MHz at 410 nm for this phototransistor. In Table 3 the bandwidths for the three presented phototransistors at $V_{CE} = -2$ V and -10 V and floating base at the three different wavelengths are shown. The upper part of the table presents the results for the $40 \times 40\ \mu m^2$ and the lower one for the $100 \times 100\ \mu m^2$ devices. Noticeable is that phototransistor $100_B Quad_E$ shows a higher bandwidth for $V_{CE} = -2$ V compared to both other phototransistors. This is caused due to a shorter diffusion distance for the generated charges. Phototransistor $100_B Edge_E$ achieves the highest bandwidth due to stronger electric field strength in the space-charge regions (see Fig. 4). However, all devices achieve a maximal bandwidth at 675 nm due to an optimal light penetration depth. Thereby the main part of the charges is generated in the thick base–collector space-charge region and thus directly in the electric field zone.

6. Conclusion

In this work we present three types of speed-optimized pnp phototransistors built in a standard 180 nm CMOS process without modifications. Each type of phototransistor was fabricated with areas of $40 \times 40\ \mu m^2$ and $100 \times 100\ \mu m^2$. For achieving high bandwidths a PIN structure was used for the base–collector junction. Hence a special starting material was used consisting of the p^+ substrate and a low doped p^- epi layer grown on top of it. By this low doped epi layer a thick space-charge region is formed, which is necessary for a fast separation of the generated charges caused by deep penetrating light. Since the phototransistors were designed for high-speed applications a further bandwidth increase was achieved by small emitter areas. This emitter area reduction leads also to a reduction of the base-emitter capacitance. However, the small emitter areas are disadvantageous for achieving high responsivities. Thus our phototransistors achieve only small dynamic responsivities up to 2.89 A/W as well as DC responsivities up to 6.44 A/W. Furthermore the phototransistors reach bandwidths up to 50.7 MHz at 850 nm, 76.9 MHz at 675 nm and 60.5 MHz at 410 nm at $V_{CE} = -10$ V and floating base conditions. These results are caused by the small capacitances and the high electric field strengths in the space-charge regions. Furthermore simulations of the electric field strengths and space-charge regions were done. Compared to the phototransistors described in [13] and [14], which were realized in 0.6 μm CMOS technology, the bandwidth is increased by more than a factor of 5. Therefore, these phototransistors are well suited for applications where a high-speed photodetector is needed with an inherent current amplification. A meaningful comparison of the presented phototransistors with other phototransistors is rather difficult since the device is strongly non-linear and its operating conditions are dependent on many factors (e.g. collector–emitter voltage, size of the device, optical light power, wavelength, additional base currents, etc.). However, the authors tried to give a comparison for 850 nm light, shown in Table 4. Possible applications for the presented phototransistors could be for example three dimensional cameras, fast opto-couplers and optical data receivers. Compared to an conventional PIN photodetector using an optimized PIN photodiode (with a responsivity of 0.4 A/W) the presented devices can be used to amplify the input signal up to a factor of 7.2, which equals an optical signal gain in the range of 8.6 dB.

Acknowledgements

Funding from the Austrian Science Fund (FWF) in the Project P21373-N22 is acknowledged.

References

[1] Zimmermann H. Integrated silicon optoelectronics. 2nd ed. Berlin, Heidelberg: Springer-Verlag; 2010.
[2] Geist J, Zalewski EF. The quantum yield of silicon in the visible. Appl Phys Lett 1979;35(7):503–6.

[3] Christensen O. Quantum efficiency of the internal photoelectric effect in silicon and germanium. J Appl Phys 1976;47:689–95.
[4] Schroder DK, Thomas RN, Swartz JC. Free carrier absorption in silicon. IEEE J Solid-State Circuits 1978;13(1):180–7.
[5] Swoboda R, Zimmermann H. 11Gb/s monolithically integrated silicon optical receiver for 850 nm wavelength. In: IEEE international solid-state circuit conference, Digest of Technical Papers ISSCC, vol. 49; 2006. p. 240–1.
[6] Schaub JD, Li R, Csutak SM, Campbell JC. High-speed monolithic silicon photoreceivers on high resistivity and SOI substrates. IEEE J Lightwave Technol 2001;19(2):272–8.
[7] Ciftcioglu B, Zhang L, Zhang J, Marciante JR, Zuegel J, Sobolewski R, et al. Integrated silicon PIN photodiodes using deep N-well in a standard 0.18-μm CMOS technology. IEEE J Lightwave Technol 2009;27(15):3303–13.
[8] Davidovic M, Zach G, Schneider-Hornstein K, Zimmermann H. TOF range finding sensor in 90 nm CMOS capable of suppressing 180 klx ambient light. IEEE Sensors 2010:2413–6.
[9] Cova S, Ghioni M, Lacaita A, Samori C, Zappa F. Avalanche photodiodes and quenching circuits for single-photon detection. Appl Opt 1996;35(12): 1956–76.
[10] Pancheri L, Stoppa D. Low-noise single photon avalanche diodes in 0.15 μm CMOS technology. In: European solid-state device research conference, Proceedings of ESSDERC; 2011. p. 179–82.
[11] Yin T, Pappu AM, Apsel AB. Low-cost, high-efficiency, and high-speed SiGe phototransistors in commercial BiCMOS. IEEE Photonics Technol Lett 2006;18(1):55–7.
[12] Lai KS, Huang JC, Hsu KYJ. High-responsivity photodetector in standard SiGe BiCMOS technology. IEEE Electron Device Lett 2007;28(9):800–2.
[13] Kostov P, Schneider-Hornstein K, Zimmermann H. Phototransistors for CMOS optoelectronic integrated circuits. Sens Actuators, A 2011;172:140–7.
[14] Kostov P, Gaberl W, Zimmermann H. Visible and NIR integrated phototransistors in CMOS technology. Solid-State Electron 2011;65–66:211–8.
[15] Hu A, Chodavarapu VP. CMOS optoelectronic lock-in amplifier with integrated phototransistor array. IEEE Trans Biomed Circuits Syst 2010;4(5):274–80.
[16] Kieschnick K, Zimmermann H, Seegebrecht P. Silicon-based optical receivers in BiCMOS technology for advanced optoelectronic integrated circuits. Mater Sci Semiconduct Process 2000;3:395–8.
[17] Carusone AC, Yasotharan H, Kao T. CMOS technology scaling considerations for multi-gbps optical receivers with integrated photodetectors. IEEE J Solid-State Circuits 2011;46(8):1832–42.
[18] Kostov P, Gaberl W, Zimmermann H. High-speed PNP PIN phototransistors in a 0.18 μm CMOS process, IEEE ESSDERC 2011. pp. 187–90.
[19] Sandage RW, Connelly JA. A fingerprint opto-detector using lateral bipolar phototransistors in a standard CMOS process. IEEE IEDM 1995:171–4.
[20] Zhang W, Chan M, Ko PK. A novel high-gain CMOS image sensor using floating N-well/gate tied PMOSFET. IEEE IEDM 1998:1023–5.
[21] Winstel G, Weyrich C. Optoelektronik II. Berlin, Heidelberg: Springer; 1986. p. 97.
[22] Sze SM, Ng KK. Physics of semiconductor devices. 3rd ed. New York: Wiley; 2006.
[23] Kirk CT. A theory of transistor cutoff frequency (fT) falloff at high current densities. IRE Trans Electron Devices 1962:164–74.
[24] Whittier RJ, Tremere DA. Current gain and cutoff frequency falloff at high currents. IEEE Trans Electron Devices 1969;16(1):39–57.